Carbon-coated ultrathin metallic V_5Se_8 nanosheet for high-energy-density and robust potassium storage

Chao Yang[†,‡,§], Fan Lv[§], Kang Dong[‡], Feili Lai[δ], Kangning Zhao[∀], Fu Sun[⊥,*], Shuming Dou[Δ], Qian Wang[§], Jie Xu[Δ], Panpan Zhang[#,*], Tobias Arlt[‡], Xiaodong Chen[&], Yanan Chen[Δ,*], Ingo Manke[‡], Shaojun Guo[§]

[†]Institute of Material Science and Technologies, Technical University Berlin, Strasse des 17. Juni 135, Berlin 10623, Germany

[‡]Helmholtz Centre Berlin for Materials and Energy, Hahn-Meitner-Platz 1, Berlin 14109, Germany

[§]Department of Materials Science and Engineering, College of Engineering, Peking University, Beijing 100871, China

[Δ]School of Materials Science and Engineering, Tianjin University, Tianjin, 300350, China

[⊥]Qingdao Institute of Bioenergy and Bioprocess Technology, Chinese Academy of Sciences, Qingdao 266101, China

[δ]Department of Chemistry, KU Leuven, Celestijnenlaan 200F, Leuven 3001, Belgium

[∀]Institute for Sustainable Energy/College of Science, Shanghai University, 99 Shangda Road, Shanghai, 200444, China

[&]Department of Applied Chemistry, School of Science, Xi'an Jiaotong University, Xi'an 710049, China

[#]School of Chemical Engineering, The University of Adelaide, Adelaide, SA 5005, Australia

Abstract

Earth-abundant potassium is a promising alternative to lithium in energy-storage systems, but a pivotal limitation of potassium-ion batteries (KIBs) is their relatively low capacity and inferior cycle stability. Here we report the first synthesis of ultrathin metallic V_5Se_8 nanosheets embedded in porous carbon (graphene-like V_5Se_8@C) as a superior anode for KIBs, which achieves a high reversible depotassiation capacity along with unprecedented rate performance and outstanding cycling stability (a reversible depotassiation capacity of 145 mAh g^{-1} after 800 cycles at 4 A g^{-1} with 82.9% capacity retention). The impressive performances achieved are attributed to the synergistic contributions of the NiAs-type superstructure, ultrathin nanosheet architecture, sufficient accessible active sites, multi-dimensional electronic/ionic transport pathways and significant pseudocapacitive

behaviors. Combined experimental analysis and first-principles calculations reveal fast reaction kinetics, high ionic/electronic conductivity and low diffusion barriers of K-ion in graphene-like V_5Se_8@C hybrid. *Ex-situ* characterizations confirm that V_5Se_8@C electrode undergo a reversible phase-evolution by the sequential intercalation and conversion reactions with synergistic K^+-storage mechanisms. Furthermore, by coupling with pre-treated $K_{0.5}MnO_2$ cathode, the full-cell is demonstrated to exhibit large energy density of 160.2 Wh kg^{-1} with average discharge voltage of 2.2 V and capacity retention of 86% over 200 cycles. These desirable findings demonstrate graphene-like V_5Se_8@C nanosheets hold great practical application in future grid-scale energy storage.

Keywords: V_5Se_8; ultrathin nanosheet; high energy and power; superior cycling stability; potassium-ion battery

1. Introduction

Electrical energy storage (EES) technologies are critically important for integrating the intermittent renewable energy resources into large-scale smart grids, which are beneficial to restrict the depletion of traditional fossil fuels and avoid severe environmental pollution [1-5]. Among the EES systems, state-of-the-art lithium-ion batteries (LIBs) are dominating the energy storage markets by virtue of their high reliability and energy density [6-8]. Unfortunately, the scarcity of lithium reserves in the Earth's crust (only 0.0017% in weight) and the increasing cost of lithium resources seriously impede the further popularization of LIBs in large-scale energy storage systems [5]. Sodium-ion batteries (NIBs) and potassium-ion batteries (KIBs) as the potential alternatives have recently captured tremendous attention on account of the high-abundance and low-cost of their raw materials. So far, much efforts have been devoted to NIBs and some progress has been achieved [9-12]. On the contrary, the developments of KIBs are still at an early stage, mainly due to the larger size of K^+ (1.38 Å) than that of Na^+ (1.02 Å). However, KIBs possess several advantages relative to NIBs, including the relatively lower redox potential of K^+/K couples (–2.92 V *vs.* standard hydrogen electrode, compared with −2.71 V for Na^+/Na) and fast ionic mobility of K^+ in liquid electrolyte,

implying that KIBs are predicted to achieve a higher operation potential and good rate performance [13-18]. Nevertheless, it is a bottleneck to look for suitable anode materials, which can host the large radius of K^+ and at the same time accommodate the huge volume variations during repetitive cycling. Until now, a veriety of anode materials have been studied for KIBs, such as carbonaceous materials [19-25], alloy-type materials [15,26-28], transition metal compounds [16,29-35], and organic material [36]. In general, two tricky issues, inferior rate capability and problematic cycle behaviors stemming from insufficient K^+-uptake, sluggish reaction kinetics and structure degradation of these electrodes during continuous potassiation and depotassiation processes, significantly hinder their practical applications in futuristic KIBs. In fact, there is another crucial issue limits the application of KIBs and need to be solved urgently: a low initial Coulombic efficiency (CE) is often observed in KIBs, which is mainly triggered by the nonreversible decomposition of electrolyte and subsequent formation of unstable electrode/electrolyte interface. Although various methods were applied to overcome the intrinsically deficient properties of the electrode materials [37-43], the current rate performance and cycling stability for KIBs are incomparable with the high performance of LIBs [7]. Therefore, further exploration of feasible anode candidates for KIBs with high reversible capacity as well as superior rate capability and excellent structural stability are urgently desirable but remain a great challenge.

Two-dimensional (2D) layered transition metal dichalcogenides (TMDs), which emerges as new inorganic graphene analogues, have been recently extensively investigated for KIBs due to their intriguing physical and chemical properties, as well as their unique structural features [44-47]. The interlayer gallery of layerd TMDs with weak van der Waals interaction facilitate the intercalation of K^+ without significant structural resistance, thus enabling an enhanced cycle capacity and reversibility during the cycling process. Nevertheless, practically, they usually have very limited electronic/ionic conductivity between two neighboring layers along the c-axis affect the electrochemical reaction kinetics to some extent, thus leading to relatively low utilization efficiency

of the active materials. Furthermore, due to the high surface energy of these 2D nanostructure materials, few-layered TMDs nanosheets tend to restack and aggregate, giving direct rise to rapid capacity degeneration at a high current density. In the face of this challenges, one can expect that the carbon-coated quasi-2D metallic V_5Se_8 nanosheet (V_5Se_8@C) is able to become a very attractive anode material for KIBs with the following merits. First, the metallic V_5Se_8, typically in the form of $V_{0.25}VSe_2$, possesses a distorted NiAs-type superstructure with periodically-aligned interstitial V-atoms linking the two adjacent VSe_2 monolayer building blocks (see crystal structure in **Figure 1a**), which would provides multiple diffusion pathways for electronic/ionic charge carriers, and thus improve the electronic/ionic conductivity along the c-axis direction (perpendicular to the VSe_2 monolayers). Meanwhile, such intriguing crystal structure could also further enhances the structural stability of the whole electrode during the potassiation/depotassiation processes. Second, the 2D nanoarchitecture construction combined with porous carbon coating can effectively prevent the aggregation and restacking concerns, enhance the active material/electrolyte interface reaction, provide much more electrochemically active sites, reduce ions/electrons diffusion paths and further enhance charge transport kinetics, trigger significant pseudocapacitive behavior, promote the growth of a stable solid-electrolyte interface (SEI) film, accommodate volume variation and help to maintain overall structural integrity of electrodes during the repeated cycles. Unfortunately, to the best of our knowledge, investigations on the charge storage mechanisms of the V_5Se_8@C hybrids together with its application as KIBs anode have not yet been reported.

Herein, we report the first example of designing ultrathin metallic V_5Se_8 nanosheets embedded in porous carbon layer (V_5Se_8@C) hybrids as an anode for KIBs by integrating all of the above-mentioned advantages into such a composite. By using this V_5Se_8@C hybrids, the half-cell delivers a high reversible specific depotassiation capacity (327 mAh g^{-1} at 0.1 A g^{-1} after 50 cycles) and superior rate performance (201 and 162 mAh g^{-1} at 2 and 4 A g^{-1}) as well as an improved long-term cyclability (145 mAh g^{-1} after 800 cycles at 4 A g^{-1} with a capacity retention of 82.9%). Moreover,

the underlying K^+-storage mechanism and possible phase transition of the V_5Se_8@C hybrid electrode during the discharge/charge process were extensively explored through electrochemical tests, *ex-situ* X-ray diffraction (XRD), *ex-situ* transmission electron microscopy (TEM), and first-principles calculations. In the last, by coupling with pre-treated $K_{0.5}MnO_2$ cathode, the full-cell assembled with the currently reported graphene-like V_5Se_8@C nanosheets hybrid electrode also exhibits a satisfactory electrochemical performance, demonstrating its great potential practical application in energy storage system.

2. Materials and methods

2.1. Materials preparation: First, the bulk V_5Se_8 was synthesized by a conventional solid-state selenylation method. In a typical synthesis procedure, vanadyl acetylacetonate ($VO(acac)_2$, 99%, Aladdin) and Se powder (Aladdin, 99.5%) with a stoichiometric ratio of 1:5 were mixed and ball-milled under an argon atmosphere for 2 h. Subsequently, the $VO(acac)_2$/Se precursor and Se powder were placed in a different upstream part of the tubular furnace and calcined at 800 °C for 2 h with a 1 °C min^{-1} ramp rate in a mixed H_2/Ar (5% H_2) atmosphere. After cooling to room temperature, black bulk V_5Se_8 powders were obtained. In the next step, the exfoliated V_5Se_8 nanosheets were prepared by a facile ion intercalation-assisted liquid exfoliation method [48]. Typically, 600 mg bulk V_5Se_8 powders and 3.5 mg NaOH were put into a 20 mL flask, and then a 15 mL of N-methyl-2-pyrrolidone (NMP, 99%, Sigma-Aldrich) was added as the dispersion solvent. The flask was sealed and the mixture was sonicated for 5 h in ice-bath system to prevent overheating during ultrasonication. After centrifuging at 6000 rpm for 15 min, the sediments containing the unexfoliated V_5Se_8 or some thick flakes were removed. Finally, the top 2/3 portion of the suspension were centrifugated, washed by deionized (DI) water and then freeze-dried to obtain the exfoliated V_5Se_8 nanosheets. The yield was calculated by measuring the weight of the exfoliated V_5Se_8 nanosheets in the final dispersion *via* the drying method and subsequently dividing it by the initial weight of the bulk V_5Se_8 powders precursor. The yield of suspended V_5Se_8 nanosheets was calculated to be 35−39

wt.%. For the control test, the V_5Se_8 dispersion was prepared by sonication without NaOH under the same conditions. For the preparation of V_5Se_8@C nanosheets, 80.0 mg of exfoliated V_5Se_8 nanosheets were dispersed in 30.0 mL of glucose solution (0.1 M). After strong stirring for 30 min, the obtained mixture was transferred to a Teflon-lined stainless steel autoclave and maintained at 200 °C for 24 h. After the reaction, the black precipitate was rinsed with DI water and freeze-dried. Last, the as-obtained powders were annealed at 800 °C for 2 h in N_2 atmosphere to obtain V_5Se_8@C nanosheets.

2.2. Materials characterization: Morphology and micro-structure of as-prepared samples were investigated by field-emission scanning electron microscopy (FESEM, FEI Nova-450) and transmission electron microscope (TEM, JEM-2100). X-ray diffraction patterns were collected using a high power microarea X-ray diffractometer (XRD, Bruker D8 Advance) using Cu Kα radiation. Raman spectra were collected with a Horiba JY Evolution spectrometer using a 633 nm laser source. The specific surface area and pore structure of the composite were analyzed by the N_2 adsorption isotherm at 77 K using the Micromeritics ASAP 2020 analyzer, and the samples were outgassed at 150 °C for 8 h before analysis. X-ray photoelectron spectroscopy (XPS) (ESCALAB 250) were performed to analyze the chemical properties of the products to explore electrochemical reaction mechanism. Atomic force microscopy (AFM) analysis was conducted on a Veeco MultiModeV atomic force microscope. Electronic conductivity of V_5Se_8@C nanosheets was carried out using the MET-007 four-point probe configure.

2.3. Electrochemical measurements: To perform the electrochemical measurements for KIBs, coin-type half cells (CR2032) were assembled in an Ar-filled glovebox using K metal foil as a counter electrode, glass microfiber filters (whatman，Grade GF/F) as the separator and 1 M potassium bis(fluorosulfonyl)imide (KFSI) dissolved in ethylene carbonate (EC)/diethyl carbonate (DEC) in a 1:1 volume ratio with 5 wt.% fluoroethylene carbonate (FEC) was used as the electrolyte. The working electrodes were fabricated by mixing 80 wt.% active material, 15 wt.% acetylene black and

5 wt.% polyvinylidene fluoride (PVDF) in NMP solvent, then pasted uniformly on a Cu foil. The resultant electrodes were dried in vacuum at 80 °C for 12 h followed by compressed at 15 Mpa and the mass loading of the active material was ~1.2 mg cm^{-2} for electrochemical test and ~5 mg cm^{-2} for ex-situ XRD measurements. The cells were aged for 10 h before measurements. Cyclic voltammetry (CV) and electrochemical impedance spectroscopy (EIS) analysis were both operated using a CHI660B electrochemical workstation (Chenhua, Shanghai, China). The CV scanning rates were 0.1, 0.2, 0.4, 0.8 and 1.2 mV s^{-1}. EIS were tested with an amplitude of 5 mV and a frequency range of 100 kHz to 10 mHz. Galvanostatic charge/discharge tests and galvanostatic intermittent titration technique (GITT) measurements of the half cells were performed in a voltage range of 0.01–2.6 V (K^+/K) at different current densities on a LAND CT2001A multichannel battery testing system. The GITT was measured with a pulse current of 0.1 A g^{-1} for 20 min at 2 h rest intervals to reach an equilibrium potential. All the electrochemical tests were performed at room temperature. For the *ex-situ* SEM, TEM, XPS and XRD characterizations, the working electrodes, obtained from the disassembled coin cells at various states, were washed with DEC and dried in a vacuum to remove excess solvents.

2.4. Computational methods: The calculations are conducted by the Vienna Ab-Initio Simulation Package (VASP) [49,50]. The projected augmented wave method is applied to deal with the ion-electron interaction and the electron exchange-correction energy is described by the generalized gradient approximation [51]. In the simulations, the kinetic cut-off energy is 380 eV. Based on optimized V_5Se_8 and graphene (Gr), V_5Se_8/Gr supercell is established by putting a (3×3) Gr on a (1×1) V_5Se_8 (002) surface, with an 18 Å vacuum layer applying along the z direction to remove the interaction between the neighbouring atom layers. The interface structure contains 32 Se atoms, 18 V atoms and 36 C atoms. The lattice mismatch is 5% and the lattice parameters are 12.465 and 7.214 Å, as seen in **Figure S1**. The interlayer distance between Gr and V_5Se_8 is 3.45 Å. To find the structure with global energy minimum, we firstly move the Gr monolayer along the z, y, and x

direction relative to the bottom V_5Se_8 surface. Then, the obtained structure is further relaxed by applying the conjugate gradient optimization method. The 5×5×4 and 2×3×1 *k*-points are applied for the bulk and interface calculations, respectively. The convergence criterion for residual forces is 0.03 eV/Å. The DFT-D2 method of Grimme is selected to describe the van der Waals interaction at the interface and spin-polarized calculations are considered in the simulations [52]. The climbing image nudged elastic band method (CI-NEB) has been used to determine the diffusion energy barriers and paths of a K-ion [53]. The charge distribution is described by using grid-based Bader analysis algorithm [54].

3. Results and discussion

The ultrathin V_5Se_8 nanosheets were prepared in high-yield by direct exfoliation of bulk V_5Se_8 powder *via* ultrasonication in NaOH-assisted N-methyl pyrrolidone (NMP) solution, as schematically illustrated in **Figure 1a**. In order to improve the exfoliation efficiency of bulk V_5Se_8 powder, the NMP was used as solvent originating from its surface energy is close to that of TMDs, and NaOH as an intercalator into the interlayer space in bulk V_5Se_8. During the vigorous ultrasonication procedure, tremendous energy can be generated and it could effectively break the interlayer bonding force to form the ultrathin V_5Se_8 nanosheets.

The powder XRD measurements were used to identify the crystalline structure of the bulk V_5Se_8, the exfoliated V_5Se_8 nanosheets, and the V_5Se_8@C hybrids (**Figure 1b**). All characteristic diffraction peaks can be perfectly indexed to the standard monoclinic V_5Se_8 (JCPDS card No. 18-1455) without any impurities. Nevertheless, they show notable differences in their diffraction peak densities. To be specific, the (002) diffraction peaks of the exfoliated V_5Se_8 and the V_5Se_8@C hybrids became weaker and broader compared to that of the bulk counterpart, implying successful formation of the ultrathin V_5Se_8 nanosheets. Interestingly, no any typical signals for carbon are observed in the V_5Se_8@C hybrid, which may be due to the trace amount of the carbon. However, the presence of carbon in the hybrid can be convincingly verified by the Raman analysis (**Figure S2**). Raman spectra

of the exfoliated V_5Se_8 and the V_5Se_8@C hybrids are almost identical except for the weak peaks located at 1350 and 1581 cm^{-1} (**Figure S2**), which correspond to the defect induced D-band and in-plane vibrational G-band of carbon, respectively. In addition, the I_D/I_G intensity ratio for V_5Se_8@C hybrid is calculated to be 0.95, corroborating a moderate degree of graphitization of the coating carbon. This is in favor of the improvement of the electrical conductivity. The characteristic bands at 280.4 and 406.1 cm^{-1} are similar to those observed in VSe_2 and thus they can be assigned to the in-plane E_{2g} and A_{1g} vibration modes of VSe_2, respectively, which confirms the layered arrangement of VSe_2 frame in the V_5Se_8 crystals [55]. The crystal structure of V_5Se_8 is illustrated in **Figure 1b**, which can be regarded as a superstructure consisting of well-ordered interstitial VSe_6 octahedra within the van der Waals gaps in the VSe_2 structure according to previous reports [56,57]. Since the periodically-aligned VSe_6 octahedra bridging the two neighbor VSe_2 monolayer building blocks can provide multi-dimensional transportation paths for electronic and ionic charge carriers, increased electronic and ionic conductivities in V_5Se_8 crystals can be obtained.

The detailed morphology and microstructure of the as-prepared products were then examined *via* SEM and TEM measurements. As shown in **Figure 1c**, SEM images of the exfoliated V_5Se_8 display the morphology of crumpled-film-like nanosheets with a lateral dimension ranging from 600 nm up to micrometer. These wrinkles were formed in the freeze-drying process and they can effectively prevent the agglomeration and restacking of the nanosheets, leading to a fast ion flux transport on the electrode–electrolyte interface. At higher magnification (the *inset* of **Figure 1c**), it can be observed that the surfaces of these nanosheets are smooth without any individual particles on it. Further, these crimped nanosheets are nearly transparent under the SEM electron-beam, indicative of their ultrathin nature. In contrast, the bulk V_5Se_8 is consisted of tabular particles with sizes of up to several micrometers, each consisting of tightly stacked layers (**Figure S3**). **Figure S4** shows SEM image of the exfoliation of bulk V_5Se_8 powder in NMP without the addition of NaOH and it is

surprisingly to find that the sheets are interweaved to form a bundle of agglomerated microflowers and that a large amount of unexfoliated particles are still present. Hence, one can conclude that the improved exfoliation efficiency of the bulk V_5Se_8 results from the assisting role of NaOH in NMP. In addition, the TEM image (**Figure 1d**) further confirms that the ultrathin character of the exfoliated V_5Se_8 nanosheets by the light contrast. From the high-resolution TEM image (HRTEM, **Figure 1e**) of the edge of the folded nanosheet in **Figure 1d**, the thickness of the exfoliated V_5Se_8 nanosheets was ~2.98 nm with approximately 5 atomic layers, while V_5Se_8 crystallinity was verified by the lattice spacings of 0.59 and 0.27 nm can be assigned to the (002) and (222) crystalline planes of the monoclinic V_5Se_8, respectively. Atomic force microscopy (AFM) characterizations provide further information on the thickness of the exfoliated V_5Se_8 nanosheets (**Figure 1f&S5a**). The corresponding AFM height profiles (**Figure 1f**) reveal that the average topographic height is ~3.1 nm, which is close to the evaluated value in **Figure 1e** and corroborated the ultrathin character.

To further improve the electrochemical performance of the exfoliated V_5Se_8 nanosheets, a strategy of carbon-coating by a facile solvothermal reaction followed by a post-annealing process is adopted (**Figure 1a**). After carbon coating, the overall morphology of the exfoliated V_5Se_8 nanosheets was well retained but their surface became coarser (**Figure 1g&S6**). Nevertheless, a thin layer of carbon evenly coated on the surface of V_5Se_8 nanosheets was also confirmed by the lesser transparency TEM image shown in **Figure 1h** *vs.* **Figure 1d**. The energy-dispersive X-ray spectrometry mappings of the V_5Se_8@C further substantiate the coexistence of V, Se, and C elements, which are uniformly distributed in the selected area (**Figure S7**). The interplanar spacing of 0.18 nm is corresponding well with the (620) crystallographic plane of the monoclinic V_5Se_8 phase (**Figure 1i)**. The corresponding selected area electron diffraction (SAED) pattern of V_5Se_8@C nanosheet (the *inset* of **Figure 1i**) gives the monoclinic structure, where the diffraction spot can be indexed to the (002) plane of the V_5Se_8 structure.

The result is in good agreement with the XRD results in **Figure 1b**. Moreover, a carbon layer with an average thickness of ~2 nm on the surface of the exfoliated V_5Se_8 nanosheet is clearly visible (**Figure 1i&S5b)** verifying the successful formation of the as-predicted V_5Se_8@C hybrid composite. The mass content of the carbon in the hybrid was estimated as ~9.8 wt.% with the thermogravimetric analysis (**Figure S8**). The HRTEM image unambiguously reveals that the coating carbon is consisted of fingerprint-like twisted wrinkles which possess numerous micro-pores at sub-nanometer scale. These micropores are not only beneficial for electrolyte infiltration but also could prevent the V_5Se_8 ultrathin nanosheets from self-aggregation. There isn't obvious interfacial stress/strain on the V_5Se_8@C hybrid due to the carbon grown on V_5Se_8 is amorphous, which is different from the reported vertically stacked 2D heterostructure [58]. Thus, the interfacial stress/strain is not discussed in this manuscript. Such thin conductive carbon film would be favorable to accelerate the electron transport and at the same time help to sustain structural integrity. The greatly enhanced conductivity together with the short K-ion diffusion length within nanosheets is expected to enable the V_5Se_8@C nanosheets electrode with fast reaction kinetics, thus yielding higher rate capability.

X-ray photoelectron spectroscopy (XPS) was performed to further investigate the surface chemical composition of the resulted V_5Se_8@C nanosheets. The wide full survey scan spectrum (**Figure S9a**) shows the co-existence of V, Se, C and O elements in the hybrid sample. As demonstrated in the high-resolution XPS spectrum of C 1*s* (**Figure S9b**), besides the C=C covalent bond, the trace O element is attributed to the C=O functional groups attached on the carbon surface. The high resolution Se 3*d* spectra in **Figure S9c** show two well-defined peaks at 54.8 and 55.8 eV, separately assigned to Se $3d_{5/2}$ and Se $3d_{3/2}$, which suggests that Se is in the form of Se^{2-} in the final V_5Se_8@C nanosheets [44,59]. In addition, another two weak peaks at 58.8 and 59.7 eV can be observed and they can be assigned to the Se–C bond. The peaks at 524.2 eV (V $2p_{1/2}$) and 516.3 eV (V $2p_{3/2}$) are assigned to the typical characteristics of V^{4+}, while those centered at 523.1 eV in V

$2p_{1/2}$ and 515.7 eV in V $2p_{3/2}$ are indexed to V^{3+} state (**Figure 1j**). These results further verified the formation of the as-predicted V_5Se_8@C nanosheets. The specific surface area and its diverse porosity of the V_5Se_8@C nanosheets were investigated by N_2 adsorption–desorption analysis. As depicted in **Figure S10**, the obvious hysteresis characteristic in the isotherm curve displays the existence of a multi-scale pore structure in the V_5Se_8@C nanosheets, and its specific surface area is calculated to be 176.3 $m^2\ g^{-1}$. To be more specific, the V_5Se_8@C nanosheets have a bimodal pore size distribution with big mesopore (>20 nm) generated from the abundant buffering space between the nanosheets and small pores from the coating carbon shell. The graphene-like multimodal pore nanoarchitecture can effectively increase the electroactive sites, facilitate the electron/K-ion flux transport, give rise to significant surface pseudocapacitive effect and effectively alleviate the volumetric expansion during repeated cycling. Moreover, the existence of Se–C bond can stabilize the discharging product and prevent Se from dissolving, thus greatly enhancing the cyclic stability of the electrode. Therefore, satisfactory electrochemical behaviors and superior K^+-storage efficiency of the V_5Se_8@C nanosheets can be anticipated.

The potassium storage behaviors of the as-prepared samples were evaluated by cyclic voltammetry (CV) and galvanostatic discharge/charge. CV tests of V_5Se_8@C nanosheets electrode for the first four cycles from 0.01 to 2.6 V (*vs.* K^+/K) at a scan rate of 0.1 mV s^{-1} are shown in **Figure 2a**, the initial reduction peak at 0.95 V corresponds to the intercalation of K^+ into V_5Se_8 lattice to form $K_xV_5Se_8$, and the broad peak centered at 0.64 V is related to the formation of irreversible SEI layer on the electrode surface [55,60]. The other broad cathodic peak observed at the range of 0.20−0.50 V can be attributed to the conversion of $K_xV_5Se_8$ into metallic V and K_2Se. A pronounced oxidation wave range from at around 1.5 and 2.1 V has also been detected in the following scan can be ascribed to the conversion reaction between K_2Se and V, further depotassiation and generation of V_5Se_8. Note that except the first scan, the V_5Se_8@C nanosheets always show decreased polarization in the subsequent CV curves, indicative of the

increased reaction kinetics and the effective utilization of active material due to the increasing wetting of the electrode by the electrolyte after the first cycle. From the second cycle onward, the CV curves show good reproducibility, demonstrating a good electrochemical reversibility of K^+-storage reaction in the V_5Se_8@C nanosheets electrode.

Figure 2b shows the representative discharge/charge profiles of the V_5Se_8@C nanosheets electrode in the 0.01−2.6 V window at 0.1 A g^{-1}. The voltage plateaus of discharge/charge curves are well consistent with the CV results mentioned above, further corroborating the multi-step electrochemical potassiation/depotassiation processes of the V_5Se_8@C nanosheets electrode. The high potassiation plateau can play a pivotal role in relieving the risk of dendrite formation on electrode surface over cycling [16,61]. The V_5Se_8@C electrode delivered discharge and charge capacities of 602 and 353 mAh g^{-1} in the first cycle, giving a low CE of 58.6%. The initial capacity fading and low CE value can be mainly attributed to the formation of SEI layer and the irreversible decomposition of electrolyte during potassiation/depotassiation reaction. Nevertheless, the subsequent CE values quickly reach over 78.5% from the second cycle and exceed 94.2% from the 10^{th} cycle, resulted from the formation of a stable SEI film on the electrode surface. In the following cycles, all the charge-discharge curves have no significant capacity loss, reflecting a good reversibility character of the V_5Se_8@C nanosheets in K^+-storage. Of especial note, in order to boost the initial CE of KIBs, a facile yet effective pre-potassiation strategy has been conducted and a high initial CE of 80.7% for V_5Se_8@C nanosheets electrode can be achieved (**Figure S11**).

The rate capabilities of the bulk V_5Se_8, the exfoliated V_5Se_8 nanosheets, and the V_5Se_8@C hybrids electrodes were systematically evaluated at different rates from 0.1 to 4 A g^{-1} (**Figure 2c**). For V_5Se_8@C nanosheets, upon successive cycling under varying current densities, the corresponding reversible charge capacities dropped only slightly on doubling the rates. When cycled at the current densities of 0.1, 0.2, 0.5, 1 and 2 A g^{-1}, V_5Se_8@C nanosheets anode can deliver reversible

depotassiation capacities of 328, 316, 293, 257, and 201 mAh g^{-1} after each 20 cycles, respectively, which are higher than those of bulk V_5Se_8 and exfoliated V_5Se_8 nanosheets under the same condition, revealing the excellent electrochemical reaction kinetics of V_5Se_8@C hybrid. Even at a large current density of 4 A g^{-1}, the reversible depotassiation capacity still remained at 162 mAh g^{-1}, highlighting the high-power application of the V_5Se_8@C nanosheets in KIBs. When the current density switched back to 0.1 A g^{-1} after 120 cycles, the depotassiation capacity can restore to above 319 mAh g^{-1} with a CE of >98%, suggesting the exceptional reversibility of V_5Se_8@C anode towards KIBs. For comparison, the rate capabilities of the V_5Se_8@C nanosheets prepared with different ultrasonication times were also examined (**Figure S12a**). Interestingly, it seems that there is no significant difference in the rate capability of the products obtained at 7 and 10 h sonication. The results suggest that ultrasonication time is not the major determining factor for the whole K^+ storage reaction.

Figure 2d displays the cycling stability and the corresponding CE of the V_5Se_8@C nanosheets electrode at the current density of 0.2 A g^{-1}. The depotassiation capacities increase gradually from 309 to 387 mAh g^{-1} at the end of 300 cycles, which can be attributed to the enhancing wetting of the electrode by the electrolyte at a low current density [55,62]. Meanwhile, the corresponding CE quickly approaches 96% within 20 cycles and stays the high value in the ensuing cycles. Further tests of cycling behaviors for the V_5Se_8@C nanosheets electrode over 300 cycles at various current densities of 0.5 and 1 A g^{-1} also reveal its excellent structural rigidness and reversibility in K^+-storage (**Figure S12b**). Besides, the excellent structural integrity of the V_5Se_8@C electrode is also further verified by the *ex-situ* SEM and TEM images characterized after 300 cycles at a current density of 1 A g^{-1} (**Figure S13**). It is clear that the sheet-like morphology of the V_5Se_8@C is well retained, with a thick K^+-permeable SEI layer is stable constructed on the surface of the electrode after the repetitive cycling. By contrast, the bulk V_5Se_8 electrode displays inferior cycling performance with substantial capacity attenuation (**Figure S14**), derived from the big volumetric expansion during the repeated charge/discharge processes. Furthermore, the long-term cycling

performances of the exfoliated V_5Se_8 nanosheets and the V_5Se_8@C hybrid electrodes are further evaluated, as depicted in **Figure 2e&S15**. When galvanostatistically cycled at a high current density of 4 A g^{-1}, a stable reversible depotassiation capacity of 145 mAh g^{-1} was achieved over 800 consecutive cycles with impressive capacity retention of 82.9%. The corresponding CE quickly reaches to near unity after the initial several cycles and remains the high value afterwards, indicating a high reversible potassiation-depotassiation process. In comparison, the exfoliated V_5Se_8 nanosheets electrode delivers a depotassiation capacity of only 81 mAh g^{-1} at 2 A g^{-1} after 800 cycles with a capacity loss of 47.5% (**Figure S15**), highlighting the contribution of coating carbon shell acts as a skeleton to sustain the cycling stability. To the best of our knowledge, the electrochemical performances of the graphene-like V_5Se_8@C nanosheets are better than that of some previously reported state-of-the-art results for KIBs (**Table S1**), showing attractive characters for future large-scale energy storage systems.

To explore the origin of high-rate capabilities in the V_5Se_8@C nanosheets, we performed CV tests under different sweeping rates of 0.2–1.2 mV s^{-1} to evaluate its electrochemical reaction kinetics (**Figure 3a**). All CV curves show analogous shapes with distinct redox peak and limited overpotential can be observed along with the increasing scan rates, indicating a high reversibility and fast kinetics for K^+-storage. The relationship between peak current (i) and scanning rate (υ) follows the formula: $i = a\upsilon^b$ [44,63,64], in which both a and b are constants, and b-value is determined by the slope of the log(i) *vs.* log(υ) plots (**Figure 3b**). The b-value of 0.5 denotes extreme diffusion-controlled process, while 1.0 represents the ideal pseudo-capacitive behavior. The b-values of the three redox peaks are 0.75, 0.94 and 0.73, respectively, manifesting that K^+-storage mechanism of V_5Se_8@C nanosheets involves both diffusion-controlled process and pseudo-capacitive effect. The standard error for cathodic fitting (peak 1) is 0.01434 (intercept) and 0.03523 (slope), while the Adj. R-Square value is 0.99334. For reduction peak 2 fitting, the standard error is 0.00814 (intercept) and 0.02001 (slope), while the value of Adj. R-Square is 0.99863. For anodic fitting (peak 3), the

standard error is 0.01128 (intercept) and 0.02773 (slope) while the Adj. R-Square value is 0.99563. In addition, the contribution of capacitive can be quantitatively deduced from the equation i (V) = $k_1v + k_2v^{0.5}$, where k_1v represents the capacitive fraction while $k_2v^{0.5}$ belongs to the diffusion-controlled process [65]. The pseudocapacitive contribution ratio of V_5Se_8@C nanosheets anode gradually intensifies with the increase of the scanning rate, and a very high value of 90.1% can be achieved at 1.2 mV s^{-1} as illustrated by the shaded area **(Figure S16a)**. In a control experiment, using the same analysis discussed for V_5Se_8@C nanosheets, the pseudocapacitive behaviors of bulk V_5Se_8 were studied by the CV curves obtained at different sweep rates ranging from 0.2–1.2 mV s^{-1} (**Figure S16b&S16c**). **Figure 3c** summarizes the pseudo-capacitive contribution ratios of V_5Se_8@C nanosheets and bulk V_5Se_8 electrodes at the various sweep rates. Apparently, the pseudo-capacitive contribution increases with increasing sweeping rate while the contribution of diffusion-controlled process decreases in both electrodes. Moreover, the pseudo-capacitive contributions in V_5Se_8@C nanosheets electrode seem to be always higher than the corresponding values of bulk V_5Se_8 electrode regardless of the sweeping rate. The superior pseudocapacitive behavior of V_5Se_8@C nanosheets electrode can be ascribed to the graphene-like nanoarchitecture increases the interface reaction with electrolyte, provides more electrochemically active sites and further enhance reaction kinetics, which are helpful to boost its electrochemical performance for K^+-storage.

Electrochemical impedance spectroscopy (EIS) test of the V_5Se_8@C nanosheets electrode was performed to investigate the reaction kinetics variation at different cycles, and the corresponding Nyquist plots are displayed in **Figure 3d**. All plots consist of a high-frequency depressed semicircle and a low-frequency sloping line, in which the former represents the resistance of charge transfer (R_{ct}) [44], and the latter is correlated to K-ion diffusion and phase transformation within V_5Se_8@C nanosheets. The corresponding equivalent circuit model is displayed in the *inset* of **Figure 3d**, and the fitted results are listed in **Table S2**. Apparently, the R_{ct}-value of V_5Se_8@C nanosheets electrode gradually decrease and remains stable in the following cycles, which are explained by the

improved electrochemical kinetics and effective utilization of the active material derived from microstructure change and stable SEI film formation. The K^+ chemical diffusion coefficients of V_5Se_8@C electrode are calculated to be 0.87×10^{-9} cm^2 s^{-1} before cycle, 1.39×10^{-9} cm^2 s^{-1} after the 50^{th} cycle, and 3.40×10^{-9} cm^2 s^{-1} after the 100^{th} cycle (**Figure S17a&Table S2**), implying the stable and fast diffusion kinetics of K^+ in V_5Se_8@C nanosheets during repetitive cycling. To further investigate the largely different electrochemical performance between the V_5Se_8@C nanosheets and bulk V_5Se_8 electrodes in KIBs, the EIS tests after the first cycle were also performed. As shown in **Figure S17b**, all the spectra contained a compressed semicircle in the high-frequency range and an inclined line in the lower frequency regime. The V_5Se_8@C nanosheets electrode shows a smaller semicircle after the first cycle, implying a better conductive property than the bulk V_5Se_8 counterpart. What's more, the closer inclined line toward 90° indicates an improved K^+ diffusion can be obtained in the V_5Se_8@C nanosheets electrode, thus enabling excellent high-rate pseudo-capacitive performance in the whole K^+ storage process. The electronic conductivity of V_5Se_8@C is determined to be 639 S cm^{-1} at room temperature (25 ℃), further corroborating its relatively high conductivity (**Figure S18**). These desirable results are mainly attributed to the 3D monoclinic structure of the V_5Se_8 that can provide multi-dimensional pathways for convenient electronic/ionic transport and the graphene-like hybrid nanoarchitecture that can shorten the electron/K^+ shuttling paths, thus enabling superior rate ability.

To further understand the thermodynamics and kinetics of the K^+-storage, galvanostatic intermittent titration (GITT) test was conducted after the initial cycle by applying a galvanostatic pulse of 0.1 A g^{-1} for 20 min between 2h-relaxation intervals to experimentally evaluate the reaction resistance of K^+ in V_5Se_8@C nanosheets electrode. The open-circuit-potential at the end of the relaxation interval is considered to be quasi-thermodynamically equilibrium voltage [16,55]. Multiple quasi-equilibrium potential platforms are detected in **Figure S19**, further verifying the

multistep electrochemical discharge and charge processes of V_5Se_8@C nanosheets. An obvious quasi-thermodynamic voltage hysteresis between K^+ intercalation and deintercalation is observed owing to the large strain/stress during the potassiation-depotassiation processes. The corresponding reaction resistance at different K^+ intercalation/deintercalation stages can be determined by dividing the overpotentials with the applied pulsed current density in GITT measurement (**Figure 3e**). During the discharge process, the reaction resistance progressively decreasing with more K^+ insertion, which can be attributed to the enhanced conductivity of the electrode caused by the metallic phase formation upon potassiation. There is an opposite tendency in the depotassiation process, which can be assigned to the decreasing ionic/electronic conductivity and worsening contact derived from the volume contraction and extraction of K^+. The reaction resistances of V_5Se_8@C nanosheets are consistently smaller than those of previously reported anodes for KIBs [16,27,66], which again confirms a better electrochemical kinetic behaviour of V_5Se_8@C nanosheets, thus delivering outstanding rate capability.

To further reveal the detailed working mechanisms of the V_5Se_8@C nanosheets electrode, *ex-situ* XRD was carried out at selected potassiation/depotassiation states in the second cycle of the half-cell to trace the fundamental phase transformation process (**Figure 3f**). When the voltage was decreased to 0.75 V, the overall intensity of the XRD peaks decreased and the (002) and (004) reflections for V_5Se_8 slightly shift to the left. This left-shift phenomenon is associated with the formation of non-stoichiometric K^+-intercalated compounds, corroborating the expansion and distortion of the V_5Se_8 crystal lattice during K^+ insertion. Further discharged deeply to 0.01 V, the reflection peaks of the V_5Se_8 were totally disappeared, and a series of new characteristic peaks were emerged: the ones observed at 20.0°, 32.9°, and 38.8° were, respectively, assigned to the (111), (220), and (311) crystallographic planes of K_2Se, while the diffraction peaks located at 41.2° and 48.0° were related to the metallic V phase (JCPDS card No. 88-2322), demonstrating the occurrence of conversion reaction. Finally, when charged to 2.6 V, all the diffraction peaks of V_5Se_8 can be recovered to their

original position, revealing a good reversibility of the potassiation-depotassiation process for the V_5Se_8@C nanosheets electrode. These results were further confirmed by *ex-situ* HRTEM tests. After discharged to 0.01 V, a visible interlayer spacing of 0.27 nm belonging to (220) plane of K_2Se, while the interplanar distances of 0.19 and 0.22 nm were indexed to the (200) and (111) planes of the metallic V, respectively (**Figure S20a-b**). When the electrode was fully charged to 2.6 V, the regular interplanar spacings of 0.28 nm and 0.19 nm are observed, which can be ascribed to the (222) and (620) planes of the monoclinic V_5Se_8, respectively (**Figure S20c-d**). Moreover, the electrochemical reaction is further verified by tracking the variations of V 2*p* signals at fully potassiation/depotassiation states (**Figure S21**). Based on the above-mentioned characterizations and discussions, the underlying reaction mechanism of K^+-storage within V_5Se_8@C nanosheets anode proceeds initially with the K^+ insertion into the V_5Se_8 layer to form $K_xV_5Se_8$, followed by the reversible conversion reaction to metallic V and K_2Se, which is schematically presented in **Figure 3g**.

To better understand the essence of the superior K-ion storage capability, we performed density theory functional (DFT) calculations to investigate the reaction mechanism, ionic and electronic transport properties of bulk V_5Se_8 and V_5Se_8/graphene (V_5Se_8/Gr). Charge density difference shows that charge transfer occurs at interface between Gr and V_5Se_8. As shown in **Figure 4a**, C and V atoms lose electrons while there is charge accumulation at top of Se atoms in the interface region. Bader charges results show that there is an increased charge transfer from V to Se atoms at V_5Se_8/Gr interface (1.26 electrons/atom) than that in bulk V_5Se_8 (1.21 electrons/atom), indicating that the formation of V_5Se_8/Gr hybrid slightly enhances the Se–V ionic bonding. Besides, weak Se–C ionic bonding is also revealed at interface with charge transfer of 0.009 e/atom. Compared with the electronic structure of the bulk V_5Se_8 (**Figure S22**), the obvious characteristics of the density of states of V_5Se_8/Gr hybrid are the strong peak strength and sharp peaks, which reveals the strong chemical bonding in the interface system (**Figure 4b**). In addition, the larger value at Fermi level (E_F) unveils a strong metallic bonding, which suggests the improved electronic conductivity of the

composite. This is contributed by V 3*d* states at E_F. Besides, strong covalent hybridization among V 3*d*, Se 4*p* and C 2*p* states in the energy range from –6 to 4 eV can be determined, reflecting the strong covalent bonding in the V_5Se_8/Gr composites. Therefore, there is a mix of metallic, ionic and covalent bonding in the V_5Se_8/Gr hybrid. The strong chemical bonding can result in improved structural integrity. Based on the above theoretical analysis, the formation of heterostructure can increase the electronic conductivity and structural stability, which will contribute to the rate performance and cycling stability of electrode materials during the charging and discharging processes. Furthermore, the adsorption energy (E_{ads}) of an isolated K^+ on various sites of V_5Se_8/Gr hybrid was calculated to reveal the K^+ intercalation behaviour (**Figure 4c-d&S23**). As seen in **Table S3**, the results show that it is energetically favourable to adsorb a K^+ on all these positions. Specially, it is more stable for K^+ to adsorb on V_5Se_8 surface (–3.30 eV) than at interface (–3.07 eV), in the interior of V_5Se_8 (–1.43 eV) and on Gr surface (–1.64 eV) in the V_5Se_8/Gr hybrid. In order to evaluate the thermodynamic properties of K^+ adsorption on various sites, the formation energy is also considered. As depicted in **Table S4**, the V_5Se_8/Gr composite could enhance the thermodynamic stability of K^+ adsorption on V_5Se_8 surface. Additionally, the effect of heterogeneous structures on K^+ diffusion kinetics in the bulk V_5Se_8 and V_5Se_8/Gr composites have also been investigated (**Figure 4e-h&S24**). The K^+ diffusion path in the bulk V_5Se_8 and interface system are given in **Figure 4e-f&S25**, respectively. As seen in **Figure 4g-h**, K^+ diffusion in the V_5Se_8/Gr interface system has a smaller energy barrier (0.25 eV) than that in the bulk V_5Se_8 (0.64 eV). Due to the different coordinate environment, for bulk V_5Se_8, a K^+ adsorb on the site near the top of V has a lower energy than that adsorbed on the region near the top of Se atom. In comparison, the adsorption of K^+ in V_5Se_8/Gr interface system shows an opposite trend where the site near the top of V is the saddle point. The low energy barrier will contribute to a fast K^+ diffusion in the interface system. Apart from that, K^+ diffusion coefficient in the interface system (1.08×10^{-7} cm^2 s^{-1}) is much larger than that in the bulk (8.40×10^{-14} cm^2 s^{-1}). Thus, the heterogeneous structure can noticeably improve the

rate performance of V_5Se_8@C hybrid by effectively decreasing K^+ diffusion energy barrier and increasing electronic conductivity, which is in good agreement with the enhanced rate performance of V_5Se_8@C composites in experiment.

Encouraged by the excellent performance of V_5Se_8@C nanosheets anode in half-cells, K-ion full cells were further matched with pre-treated $K_{0.5}MnO_2$ (**Figure S26**) as the cathode with the same separator and electrolyte as the half cell. The working mechanism of the full cell is schematically illustrated in **Figure 5a**, where K ions are extracted from the pre-treated $K_{0.5}MnO_2$ and inserted into the V_5Se_8@C anode during the potassiation process, and a reverse process occurs during depotassiation. As depicted in **Figure 5b**, the full-cell provides a considerable discharge capacity of 93 mAh g^{-1} for the second cycle at 0.05 A g^{-1} (based on the cathode mass) in a voltage window of 1.50–3.60 V with an average discharge voltage of 2.2 V, corresponding to an energy density of 160.2 Wh kg^{-1} (based on the total mass of both cathode and anode materials, and the mass ratio of $K_{0.5}MnO_2$: V_5Se_8@C is 3.6:1 in the full-cell), which apparently superior to most of the recently reported K-ion full battery (**Table S5**). Furthermore, there is no significant capacity attenuation in the discharge capacity between the 10^{th} and 30^{th} cycles at the low current density, suggesting a good reaction reversibility and an outstanding electrochemical stability. **Figure 5c** presents the rate capability of the full cell, which delivers reversible discharge capacities of 99, 87, 80, 72 and 60 mAh g^{-1} at a current rate from 0.02 to 0.4 A g^{-1}. When the current density recovered to 0.05 A g^{-1}, the discharge capacity returned back to 75 mAh g^{-1}, implying a reasonable rate performance of V_5Se_8@C nanosheets in the full cell. Moreover, the round-trip efficiency of present full-cell is 81.3% (**Figure 5d**), which is almost equivalent with the reported value for NIBs [67]. It is worth mentioning that the as-prepared full battery after a long-term cycling could easily make the commercial LED lights shine (**Figure 5e**). Besides, the as-fabricated $K_{0.5}MnO_2$//V_5Se_8@C full cell also exhibits a prominent durability at various current densities from 0.2 to 0.3 A g^{-1}, as shown in **Figure S27**. **Figure 5f** displays the cycling stability test of the full-cell at a current density of 0.4 A g^{-1}. After 200

cycles, the full cell retains 86% of its initial capacity with an average CE ~95.3%, manifesting the considerable cycling stability of our full battery. Such exceptional K^+-storage performance suggests promising practical applications of the graphene-like V_5Se_8@C nanosheets in full KIBs for energy storage.

4. Conclusion

In summary, graphene-like V_5Se_8@C nanosheets hybrid were obtained in high-yield by a facile exfoliation strategy and subsequent solvothermal treatment, and investigated for the first time as an advanced anode for KIBs. On the one hand, the metallic V_5Se_8 exhibits a NiAs-type superstructure with ordered interstitial V atoms linked the two neighbor VSe_2 monolayer building blocks, which would not only provide multi-dimensional pathways for convenient electronic and ionic transportation, but also improve their structure durability. On the other hand, graphene-like nanostructure combined with porous carbon coating layer can effectively prevent the aggregation of the active material, increase the electrode/electrolyte interface area, provide abundant electrochemically active sites for K^+-storage, facilitate fast transportation of K-ion/electron, give rise to significant pseudocapacitive-like electrochemical behavior, accommodate volume expansion and help to sustain overall structural integrity of electrode during repetitive cycling. Owing to the multiple collaborative effects of the aforementioned advantages, the V_5Se_8@C nanosheets electrode shows an impressive reversible depotassiation capacity (327 mAh g^{-1} at 0.1 A g^{-1} after 50 cycles), splendid rate capability (201 and 162 mAh g^{-1} at 2 and 4 A g^{-1}) , and prominent long-term cycling stability (82.9% capacity retention over 800 cycles at 4 A g^{-1}). Systematical experimental characterizations and first-principles calculations bring insights into the intrinsic correlations between the electrochemical reaction kinetics and the K^+-storage mechanisms of the V_5Se_8@C electrode. Particularly noteworthy, pairing this V_5Se_8@C nanosheets anode with a pre-treated $K_{0.5}MnO_2$ cathode yields a potassium-ion full cell with a large energy density of 160.2 Wh kg^{-1},

impressive rate performance and negligible capacity decay within 200 cycles, revealing the great application potential of V_5Se_8@C nanosheets in future grid-scale energy storage.

Conflict of Interest Statement

The authors declare no competing financial interests.

Supporting Information

Supplementary data associated with this article can be found in the online version at doi:10.1016/j.ensm. Additional SEM, TEM, XRD, XPS, TGA, first-principles calculations and electrochemical performance.

Corresponding Authors

*E-mail: sunfu@qibebt.ac.cn.

*E-mail: panpan.zhang@postgrad.curtin.edu.au.

*E-mail: yananchen@tju.edu.cn.

Acknowledgements

This work was financially supported by the National Natural Science Foundation of China (Grant No. 91963113, 51671003, 51802007 and U1904216), the Helmholtz Association, the China Scholarship Council (CSC) and was partially funded by the German Research Foundation (DFG, Project No. MA 5039/4-1). The simulation was supported by resources provided by the Pawsey Supercomputing Centre with funding from the Australian Government and the Government of Western Australia.

References

(1) K. Lin, Q. Chen, M. Gerhardt, L. Tong, S. Kim, L. Eisenach, A. Valle, D. Hardee, R. Gordon, M. Aziz, Alkaline quinone flow battery, Science 349 (2015) 1529–1532.

(2) J. Choi, D. Aurbach, Promise and Reality of Post-Lithium-Ion Batteries with High Energy Densities. Nat. Rev. Mater. 1 (2016) 16013.

(3) J. Xu, F. Yu, J. Hua, W. Tang, C. Yang, S. Hu, S. Zhao, X. Zhang, Z. Xin, D. Niu, Donor Dominated Triazine-Based Microporous Polymer as a Polysulfide Immobilizer and Catalyst for High-Performance Lithium-Sulfur Batteries. Chem. Eng. J. 392 (2019) 123694.

(4) S. Chu, Y. Cui, N. Liu, The Path Towards Sustainable Energy. Nat. Mater. 16 (2016) 16–22.

(5) B. Ji, F. Zhang, X. Song, Y. Tang, A Novel Potassium-Ion-Based Dual-Ion Battery. Adv. Mater. 29 (2017) 1700519.

(6) Z. Tian, N. Chui, R. Lian, Q. Yang, W. Wang, C. Yang, D. Rao, J. Huang, Y. Zhang, F. Lai, C. Liu, T. Liu, Dual Anionic Vacancies on Carbon Nanofiber Threaded MoSSe Arrays: A Free-Standing Anode for High-Performance Potassium-Ion Storage. Energy Storage Mater. 27 (2020) 591–598.

(7) D. Larcher, J. Tarascon, Towards Greener and More Sustainable Batteries for Electrical Energy Storage. Nat. Chem. 7 (2015) 19–29.

(8) L. Shen, Y. Wang, H. Lv, S. Chen, P. van Aken, X. Wu, J. Maier, Y. Yu, Ultrathin $Ti_2Nb_2O_9$ Nanosheets with Pseudocapacitive Properties as Superior Anode for Sodium-Ion Batteries. Adv. Mater. 30 (2018) 1804378.

(9) N. Wang, Z. Bai, Y. Qian, J. Yang, Double-Walled Sb@TiO_{2-x} Nanotubes as a Superior High-Rate and Ultralong-Lifespan Anode Material for Na-Ion and Li-Ion Batteries. Adv. Mater. 28 (2016) 4126–4133.

(10) S. Chen, C. Wu, L. Shen, C. Zhu, Y. Huang, K. Xi, J. Maier, Y. Yu, Challenges and Perspectives for NASICON-Type Electrode Materials for Advanced Sodium-Ion Batteries. Adv. Mater. 29 (2017) 1700431.

(11) C. Chen, Y. Wen, X. Hu, X. Ji, M. Yan, L. Mai, P. Hu, B. Shan, Y. Huang, Na^+ Intercalation Pseudocapacitance in Graphene-Coupled Titanium Oxide Enabling Ultra-Fast Sodium Storage and Long-Term Cycling. Nat. Commun. 6 (2015) 6929.

(12) J. Yang, S. Xiao, X. Cui, W. Dai, X. Lian, Z. Hao, Y. Zhao, J. Pan, Y. Zhou, L. Wang, W. Chen, Inorganic-Anion-Modulated Synthesis of 2D Nonlayered Aluminum-Based Metal-Organic Frameworks as Carbon Precursor for Capacitive Sodium Ion Storage. Energy Storage Mater. 26 (2020) 391−399.

(13) W. Wang, J. Zhou, Z. Wang, L. Zhao, P. Li, Y. Yang, C. Yang, H. Huang, S. Guo, Short-Range Order in Mesoporous Carbon Boosts Potassium-Ion Battery Performance. Adv. Energy Mater. 8 (2018) 1701648.

(14) J. Zheng, Y. Yang, X. Fan, G. Ji, X. Ji, H. Wang, S. Hou, M. Zachariah, C. Wang, Extremely Stable Antimony-Carbon Composite Anodes for Potassium-Ion Batteries. Energy Environ. Sci. 12 (2019) 615–623.

(15) P. Xiong, P. Bai, A. Li, B. Li, M. Cheng, Y. Chen, S. Huang, Q. Jiang, X. Bu, Y. Xu, Bismuth Nanoparticle@Carbon Composite Anodes for Ultralong Cycle Life and High-Rate Sodium-Ion Batteries. Adv. Mater. 31 (2019) 1904771.

(16) C. Yang, J. Feng, Y. Zhang, Q. Yang, P. Li, T. Arlt, F. Lai, J. Wang, C. Yin, W. Wang, G. Qian, L. Cui, W. Yang, Y. Chen, I. Manke, Multidimensional Integrated Chalcogenides Nanoarchitecture Achieves Highly Stable and Ultrafast Potassium-Ion Storage. Small 15 (2019) 1903720.

(17) C. Yang, F. Lv, Y. Zhang, J. Wen, K. Dong, H. Su, F. Lai, G. Qian, W. Wang, A. Hilger, Y. Xu, Y. Zhu, Y. Deng, W. Hu, I. Manke, Y. Chen, Confined Fe_2VO_4⊂Nitrogen-Doped Carbon Nanowires with Internal Void Space for High-Rate and Ultrastable Potassium-Ion Storage. Adv. Energy Mater. 9 (2019) 1902674.

(18) J. Ding, H. Zhang, H. Zhou, J. Feng, X. Zheng, C. Zhong, E. Paek, W. Hu, D. Mitlin, Sulfur-Grafted Hollow Carbon Spheres for Potassium-Ion Battery Anodes. Adv. Mater. 31 (2019) 1900429.

(19) Y. Li, C. Yang, F. Zheng, X. Ou, Q. pan, Y. Liu, G. wang, High Pyridine N-Doped Porous Carbon Derived from Metal–Organic Frameworks for Boosting Potassium-Ion Storage. J. Mater. Chem. A 6 (2018) 17959–17966.

(20) Y. Xie, Y. Chen, L. Liu, P. Tao, M. Fan, N. Xu, X. Shen, C. Yan, Ultra-High Pyridinic N-Doped Porous Carbon Monolith Enabling High-Capacity K-Ion Battery Anodes for Both Half-Cell and Full-Cell Applications. Adv. Mater. 29 (2017) 1702268.

(21) Y. Xu, C. Zhang, M. Zhou, Q. Fu, C. Zhao, M. Wu, Y. Lei, Highly Nitrogen Doped Carbon Nanofibers with Superior Rate Capability and Cyclability for Potassium Ion Batteries. Nat. Commun. 9 (2018) 1720.

(22) Z. Jian, Z. Xing, C. Bommier, Z. Li, X. Ji, Hard Carbon Microspheres: Potassium-Ion Anode Versus Sodium-Ion Anode. Adv. Energy Mater. 6 (2016) 1501874.

(23) J. Yang, Z. Ju, Y. Jiang, Z. Xing, B. Xi, J. Feng, S. Xiong, Enhanced Capacity and Rate Capability of Nitrogen/Oxygen Dual-Doped Hard Carbon in Capacitive Potassium-Ion Storage. Adv. Mater. 30 (2018) 1700104.

(24) K. Share, A. Cohn, R. Carter, B. Rogers, C. Pint, Role of Nitrogen-Doped Graphene for Improved High-Capacity Potassium Ion Battery Anodes. ACS Nano 10 (2016) 9738–9744.

(25) J. Zhang, T. Liu, X. Cheng, M. Xia, R. Zheng, N. Peng, H. Yu, M. Shui, J. Shu, Development Status and Future Prospect of Non-Aqueous Potassium Ion Batteries for Large Scale Energy Storage. Nano Energy 60 (2019) 340–361.

(26) B. Wang, Z. Deng, Y. Xia, J. Hu ,H. Li, H. Wu, Q. Zhang, Y. Zhang, H. Liu, S. Dou, Realizing Reversible Conversion-Alloying of Sb(V) in Polyantimonic Acid for Fast and Durable Lithium- and Potassium-Ion Storage. Adv. Energy Mater. 10 (2020) 1903119.

(27) P. Xiong, P. Bai, S. Tu, M. Cheng, J. Zhang, J. Sun, Y. Xu, Red Phosphorus Nanoparticle@3D Interconnected Carbon Nanosheet Framework Composite for Potassium-Ion Battery Anodes. Small 14 (2018) 1802140.

(28) W. Zhang, W. Pang, V. Sencadas, Z. Guo, Understanding High-Energy-Density Sn_4P_3 Anodes for Potassium-Ion Batteries. Joule 2 (2018) 1534–1547.

(29) Q. Yu, B. Jiang, J. Hu, C. Lao, Y. Gao, P. Li, Z. Liu, G. Suo, D. He, W. Wang, G. Yin, Metallic Octahedral $CoSe_2$ Threaded by N-Doped Carbon Nanotubes: A Flexible Framework for High-Performance Potassium-Ion Batteries. Adv. Sci. 5 (2018) 1800782.

(30) H. Gao, T. Zhou, Y. Zheng, Q. Zhang, Y. Liu, J. Chen, H. Liu, Z. Guo, CoS Quantum Dot Nanoclusters for High-Energy Potassium-Ion Batteries. Adv. Funct. Mater. 27 (2017) 1702634.

(31) J. Zhou, H, Zhao, Q. Zhang, T. Li, Y. Li, N. Lin, Y. Qian, Carbon Nanotube-Stabilized Co_9S_8 Dual-Shell Hollow Spheres for High-Performance K-Ion Storage. Chem. Commun. 55 (2019) 1406–1409.

(32) H. Lin, M. Li, X. Yang, D. Yu, Y. Zeng, C. Wang, G. Chen, F. Du, Nanosheets-Assembled CuSe Crystal Pillar as a Stable and High-Power Anode for Sodium-Ion and Potassium-Ion Batteries. Adv. Energy Mater. 9 (2019) 1900323.

(33) Y. Zhao, J. Zhu, S. Ong, Q. Yao, X. Shi, K. Hou, Z. J. Xu, L. Guan, High-Rate and Ultralong Cycle-Life Potassium Ion Batteries Enabled by In Situ Engineering of Yolk-Shell FeS_2@C Structure on Graphene Matrix. Adv. Energy Mater. 8 (2018) 1802565.

(34) Y. He, L. Wang, C. Dong, C. Li, X. Ding, Y. Qian, L. Xu, In Situ Rooting ZnSe/N-Doped Hollow Carbon Architectures as High-Rate and Long-Life Anode Materials for Half/Full Sodium-Ion and Potassium-Ion Batteries. Energy Storage Mater. 23 (2019) 35–45.

(35) X. Xu, B. Mai, Z. Liu, S. Ji, R. Hu, L. Ouyang, J. Liu, M. Zhu, Self-Sacrificial Template-Directed ZnSe@C as High Performance Anode for Potassium-Ion Batteries. Chem. Eng. J. 387 (2020) 124061.

(36) C. Zhang, Y. Qiao, P. Xiong, W. Ma, P. Bai, X. Wang, Q. Li, J. Zhao, Y. Xu, Y. Chen, J. Zeng, F. Wang, Y. Xu, J. Jiang, Conjugated Microporous Polymers with Tunable Electronic Structure for High-Performance Potassium-Ion Batteries. ACS Nano 13 (2019) 745–754.

(37) Y. Dong, Y. Xu, W. Li, Q. Fu, M. Wu, E. Manske, J. Kröger, Y. Lei, Insights into the Crystallinity of Layer-Structured Transition Metal Dichalcogenides on Potassium Ion Battery Performance: A Case Study of Molybdenum Disulfide. Small 15 (2019) 1900497.

(38) D. Adekoya, M. Li, M. Hankel, C. Lai, M. Balogun, Y. Tong, S. Zhang, Design of a 1D/2D C_3N_4/rGO Composite as an Anode Material for Stable and Effective Potassium Storage. Energy Storage Mater. 25 (2020) 495–501.

(39) D. Adekoya, H. Chen, H. Hoh, T. Gould, M. Balogun, C. Lai, H. Zhao, S. Zhang, Hierarchical Co_3O_4@N-Doped Carbon Composite as an Advanced Anode Material for Ultra-Stable Potassium Storage. ACS Nano 14 (2020) 5027–5035.

(40) H. Huang, J. Cui, G. Liu, R. Bi, L. Zhang, Carbon-Coated $MoSe_2$/MXene Hybrid Nanosheets for Superior Potassium Storage. ACS Nano 13 (2019) 3448−3456.

(41) H. Yu, X. Cheng, M. Xia, T. Liu, W. Ye, R. Zheng, N. Long, M. Shui, J. Shu, Pretreated Commercial $TiSe_2$ as an Insertion-Type Potassium Container for Constructing “Rocking-Chair” Type Potassium Ion Batteries. Energy Storage Mater. 22 (2019) 154−159.

(42) H. Fan, X. Wang, H. Yu, Q. Gu, S. Chen, Z. Liu, X. Chen, W. Luo, H. Liu, Enhanced Potassium Ion Battery by Inducing Interlayer Anionic Ligands in $MoS_{1.5}Se_{0.5}$ Nanosheets with Exploration of the Mechanism. Adv. Energy Mater. 10 (2020) 1904162.

(43) C. Etogo, H. Huang, H. Hong, G. Liu, L. Zhang, Metal–Organic-Frameworks-Engaged Formation of $Co_{0.85}Se$@C Nanoboxes Embedded in Carbon Nanofibers Film for Enhanced Potassium-Ion Storage. Energy Storage Mater. 24 (2020) 167−176.

(44) C. Yang, J. Feng, F. Lv, J. Zhou, C. Lin, K. Wang, Y. Zhang, Y. Yang, W. Wang, J. Li, S. Guo, Metallic Graphene-Like VSe_2 Ultrathin Nanosheets: Superior Potassium-Ion Storage and Their Working Mechanism. Adv. Mater. 30 (2018) 1800036.

(45) H. Tian, X. Yu, H. Shao, L. Dong, Y. Chen, X. Fang, C. Wang, W. Han, G. Wang, Unlocking Few-Layered Ternary Chalcogenides for High-Performance Potassium-Ion Storage. Adv. Energy Mater. 9 (2019) 1901560.

(46) Y. Cui, W. Liu, W. Feng, Y. Zhang, Y. Du, S. Liu, H. Wang, M. Chen, J. Zhou, Controlled Design of Well-Dispersed Ultrathin MoS_2 Nanosheets Inside Hollow Carbon Skeleton: Toward Fast Potassium Storage by Constructing Spacious "Houses" for K Ions. Adv. Funct. Mater. 30 (2020) 1908755.

(47) J. Ge, L. Fan, J. Wang, Q. Zhang, Z. Liu, E. Zhang, Q. Liu, X. Yu, B. Lu, Nature of $FeSe_2$/N-C Anode for High Performance Potassium Ion Hybrid Capacitor. Adv. Energy Mater. 8 (2018) 1801477.

(48) C. Tan, X. Cao, X. Wu, Q. He, J. Yang, X. Zhang, J. Chen, W. Zhao, S. Han, G. Nam, M. Sindoro, H. Zhang, Recent Advances in Ultrathin Two-Dimensional Nanomaterials. Chem. Rev. 117 (2017) 6225−6331.

(49) G. Kresse, J. Furthmüller, Efficiency of Ab-Initio Total Energy Calculations for Metals and Semiconductors Using A Plane-Wave Basis Set. Comput. Mater. Sci. 6 (1996) 15–50.

(50) G. Kresse, J. Furthmüller, Self-Interaction Correction to Density Functional Approximation for Many Electron Systems. Phys. Rev. B 54 (1996) 11169–11186.

(51) J. Perdew, K. Burke, M. Ernzerhof, Generalized Gradient Approximation Made Simple. Phys. Rev. Lett. 77 (1996) 3865–3868.

(52) S. Grimme, Semiempirical GGA-Type Density Functional Constructed with a Long-Range Dispersion Correction. J. comput. chem. 27 (2006) 1787–1799.

(53) G. Henkelman, B. Uberuaga, H. Jónsson, A Climbing Image Nudged Elastic Band Method for Finding Saddle Points and Minimum Energy Paths. J. chem. phys. 113 (2000) 9901–9904.

(54) G. Henkelman, A. Arnaldsson, H. Jónsson, A Fast and Robust Algorithm for Bader Decomposition of Charge Density. Comput. Mater. Sci. 36 (2006) 354–360.

(55) F. Ming, H. Liang, Y. Lei, W. Zhang, H. Alshareef, Solution Synthesis of VSe_2 Nanosheets and Their Alkali Metal Ion Storage Performance. Nano Energy 53 (2018) 11–16.

(56) C. Yang, X. Ou, X. Xiong, F. Zheng, R. Hu, Y. Chen, M. Liu, K. Huang, V_5S_8-Graphite Hybrid Nanosheets as a High Rate-Capacity and Stable Anode Material for Sodium-Ion Batteries. Energy Environ. Sci. 10 (2017) 107–113.

(57) L. Li, W. Zhang, X. Wang, S. Zhang, Y. Liu, M. Li, G. Zhu, Y. Zheng, Q. Zhang, T. Zhou, W. K. Pang, W. Luo, Z. Guo, J. Yang, Hollow-Carbon-Templated Few-Layered V_5S_8 Nanosheets Enabling Ultrafast Potassium Storage and Long-Term Cycling. ACS Nano 13 (2019) 7939–7948.

(58) L. Oakes, R. Carter, T. Hanken, A. Cohn, K. Share, B. Schmidt, C. Pint, Interface Strain in Vertically Stacked Two-Dimensional Heterostructured Carbon-MoS_2 Nanosheets Controls Electrochemical Reactivity. Nat. Commun. 7 (2016) 11796.

(59) B. Li, Z. He, J. Zhao, W. Liu, Y. Feng, J. Song, Advanced Se_3P_4@C Anode with Exceptional Cycling Life for High Performance Potassium-Ion Batteries. Small 16 (2020) 1906595.

(60) Z. Tian, N. Chui, R. Lian, Q. Yang, W. Wang, C. Yang, D. Rao, J. Huang, Y. Zhang, F. Lai, C. Liu, T. Liu, Dual Anionic Vacancies on Carbon Nanofiber Threaded MoSSe Arrays: A Free-Standing Anode for High-Performance Potassium-Ion Storage. Energy Storage Mater. 27 (2020) 591–598.

(61) Z. Jian, W. Luo, X. Ji, Carbon Electrodes for K-Ion Batteries. J. Am. Chem. Soc. 137 (2015) 11566–11569.

(62) J. Zhou, L. Wang, M. Yang, J. Wu, F. Chen, W. Huang, N. Han, H. Ye, F. Zhao, Y. Li, Y. Li, Hierarchical VS_2 Nanosheet Assemblies: A Universal Host Material for the Reversible Storage of Alkali Metal Ions. Adv. Mater. 29 (2017) 1702061.

(63) C. Yang, S. Yu, C. Lin, F. Lv, S. Wu, Y. Yang, W. Wang, Z. Zhu, J. Li, N. Wang, S. Guo, $Cr_{0.5}Nb_{24.5}O_{62}$ Nanowires with High Electronic Conductivity for High-Rate and Long-Life Lithium-Ion Storage. ACS Nano 11 (2017) 4217–4224.

(64) Y. Liu, Z. Sun, X. Sun, Y. Lin, K. Tan, J. Sun, L. Liang, L. Hou, C. Yuan, Construction of Hierarchical Nanotubes Assembled from Ultrathin V_3S_4@C Nanosheets Towards Alkali-Ion Batteries with Ion-Dependent Electrochemical Mechanisms. Angew. Chem. Int. Ed. 59 (2020) 2473–2482.

(65) W. Zong, C. Yang, L. Mo, Y. Ouyang, H. Guo, L. Ge, Y. Miao, D. Rao, J. Zhang, F. Lai, T. Liu, Elucidating Dual-Defect Mechanism in Rhenium Disulfide Nanosheets with Multi-Dimensional Ion Transport Channels for Ultrafast Sodium Storage. Nano Energy 77 (2020) 105189.

(66) P. Xiong, X. Zhao, Y. Xu, Nitrogen-Doped Carbon Nanotubes Derived from Metal-Organic Frameworks for Potassium-Ion Battery Anodes. ChemSusChem 11 (2018) 202–208.

(67) L. Mu, S. Xu, Y. Li, Y.-S. Hu, H. Li, L. Chen, X. Huang, Prototype Sodium-Ion Batteries Using an Air-Stable and Co/Ni-Free O3-Layered Metal Oxide Cathode. Adv. Mater. 27 (2015) 6928–6933.

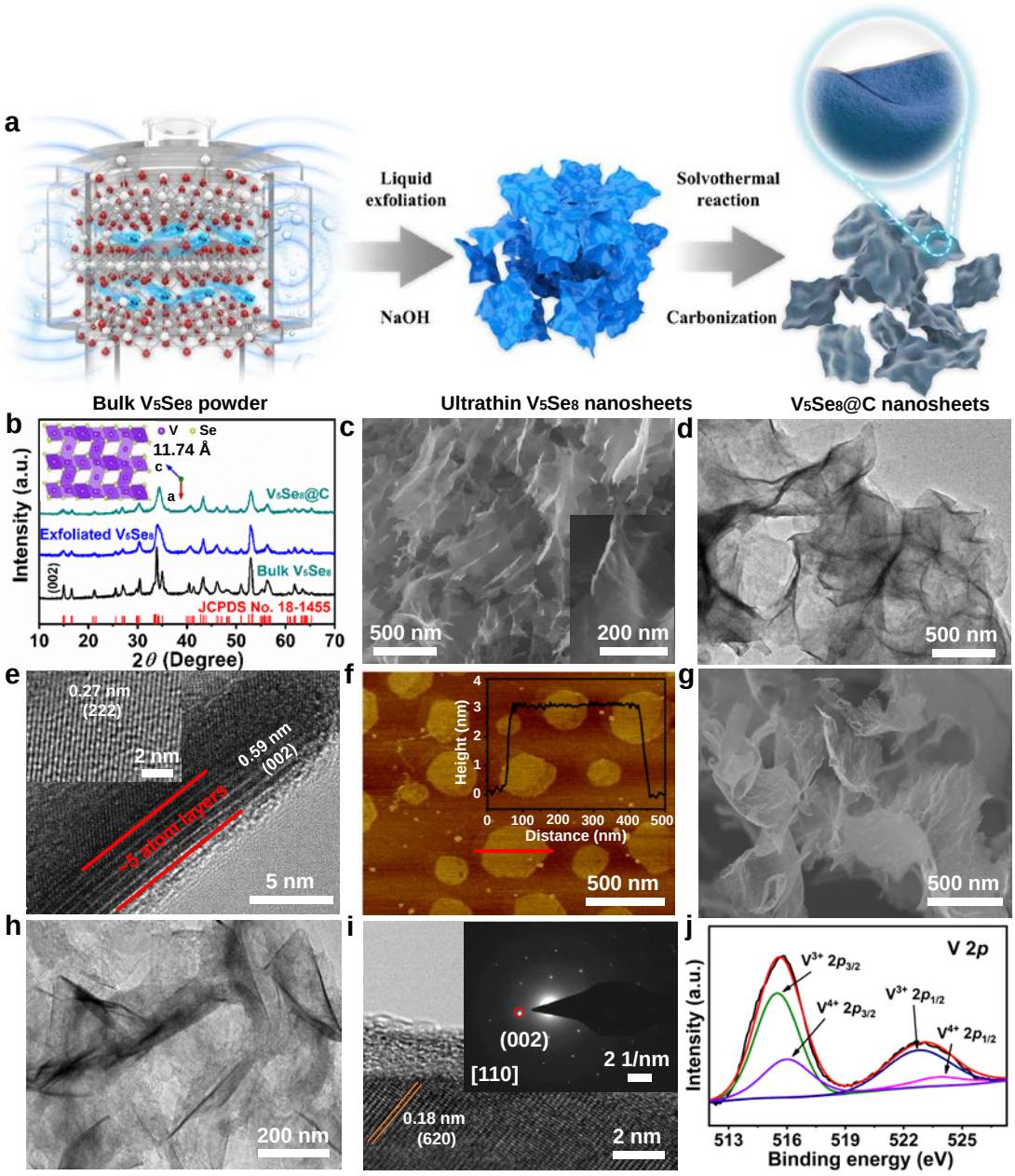

Figure 1. (a) Schematic illustration of the preparation process of the graphene-like V_5Se_8@C nanosheets. (b) XRD patterns of bulk V_5Se_8, exfoliated V_5Se_8 nanosheets, and V_5Se_8@C hybrids. Inset is the side-view of atoms arrangements in V_5Se_8. The purple (big) and yellow (small) balls represent V and Se atoms, respectively. SEM (c) and TEM (d, e) images of the exfoliated V_5Se_8 nanosheets. The *inset* of (c) is high-magnification SEM, and the *inset* of (e) is the HRTEM images of the exfoliated V_5Se_8 nanosheets. (f) Representative AFM image of the exfoliated V_5Se_8 nanosheets and the corresponding linear scan analysis. (g) SEM image, (h) TEM image, (i) HRTEM image of the graphene-like V_5Se_8@C nanosheets. The HRTEM image viewed from the [001] direction. The

inset of (i) is the corresponding SAED pattern. (j) XPS high-resolution V 2*p* spectra of the V_5Se_8@C nanosheets.

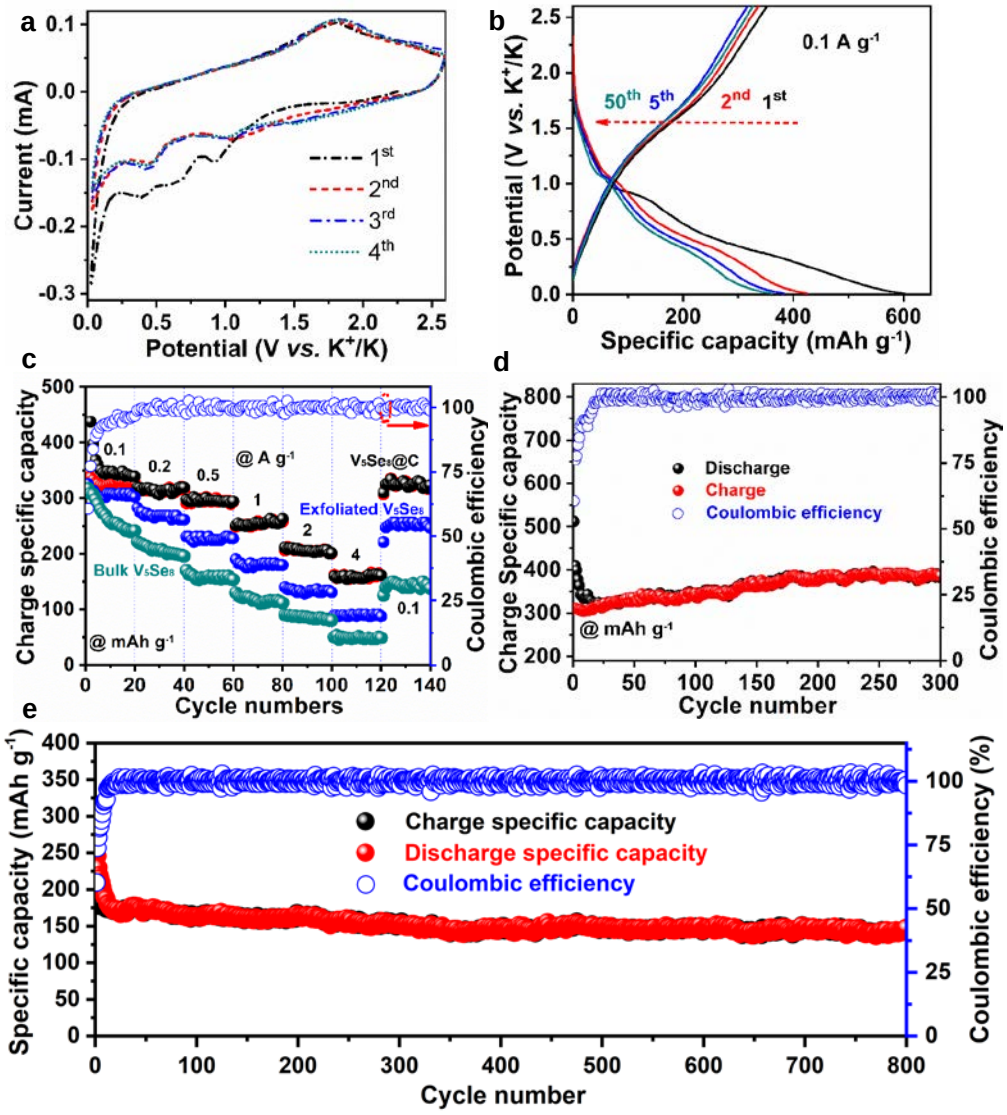

Figure 2. (a) CV curves for the graphene-like V_5Se_8@C nanosheets electrode in the first four cycles at a scan rate of 0.1 mV s^{-1}. (b) Galvanostatic discharging/charging profiles for the V_5Se_8@C nanosheets at different cycles at 0.1 A g^{-1}. (c) Rate capabilities of the bulk V_5Se_8, exfoliated V_5Se_8 nanosheets, and V_5Se_8@C hybrid electrodes at various current densities from 0.1 to 4 A g^{-1}. (d) Cycling stability and corresponding CE of the V_5Se_8@C nanosheets electrode at 0.2 A g^{-1}. (e) The cycling performance and CE of the V_5Se_8@C nanosheets electrode for 800 cycles at 4 A g^{-1}. (Note that all the specific capacity values of half cell were calculated based on the total mass of the anode material).

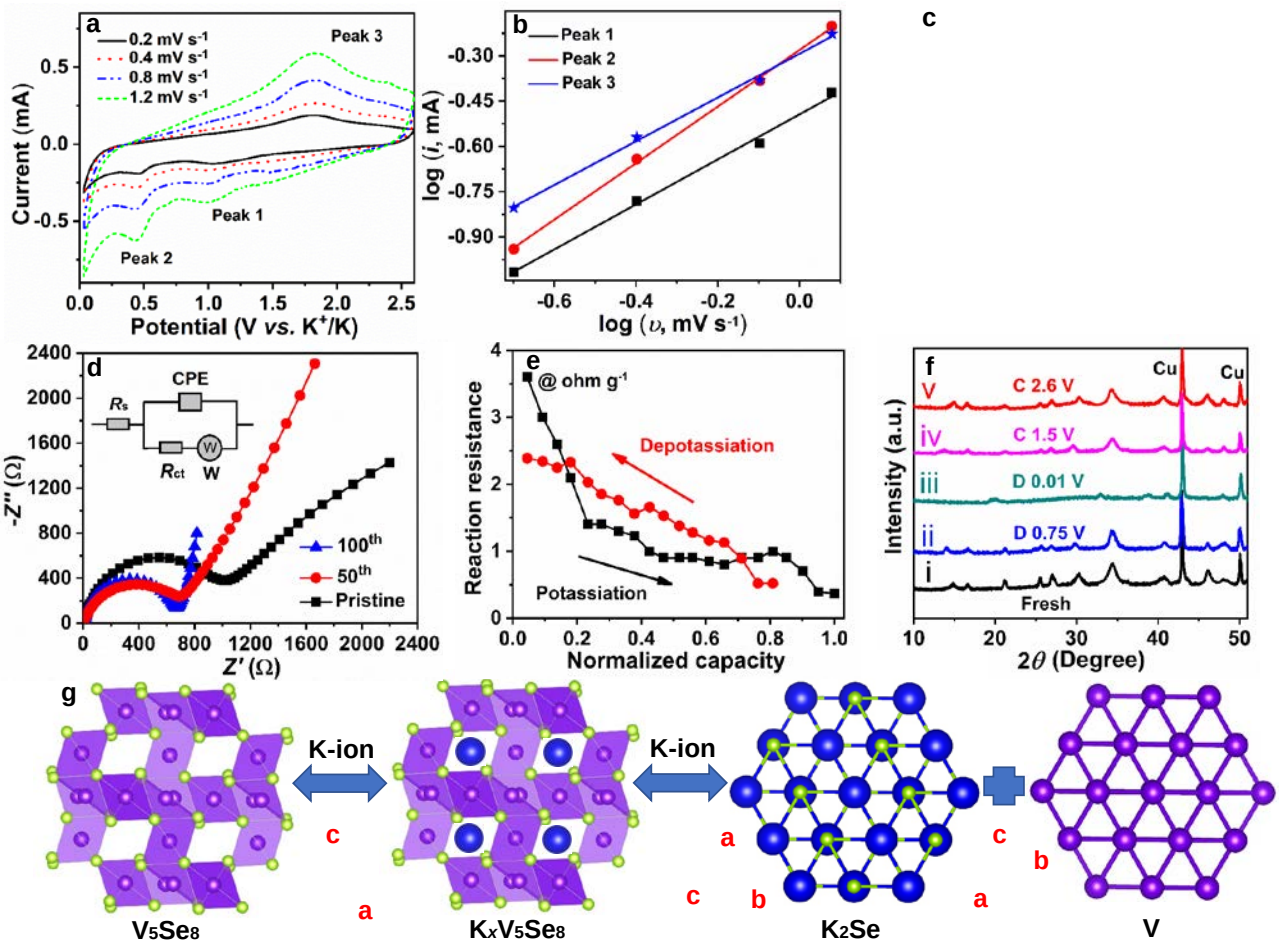

Figure 3. (a) CV profiles at different scan rates and (b) the plots of log(*i*) *vs.* log(*υ*) at each redox-peak pair (peak current: *i*, scan rate: *υ*) of the V_5Se_8@C nanosheets electrode. (c) The percentages of K-ion diffusion controlled and pseudocapacitive contributions at different scanning rates of V_5Se_8@C nanosheets and bulk V_5Se_8 electrodes. (d) Nyquist plots of V_5Se_8@C nanosheets electrodes after different cycles (inset: selected equivalent circuit). (e) Reaction resistance during potassiation/depotassiation processes of V_5Se_8@C nanosheets electrode in KIBs. (f) *Ex-situ* XRD patterns of V_5Se_8@C nanosheets electrodes at the different state (D: state of discharge, C: state of charge). (g) Schematic illustration of reversible potassiation/depotassiation process in the graphene-like V_5Se_8@C nanosheets electrode. The purple, yellow, and blue spheres represent V, Se and K atoms, respectively.

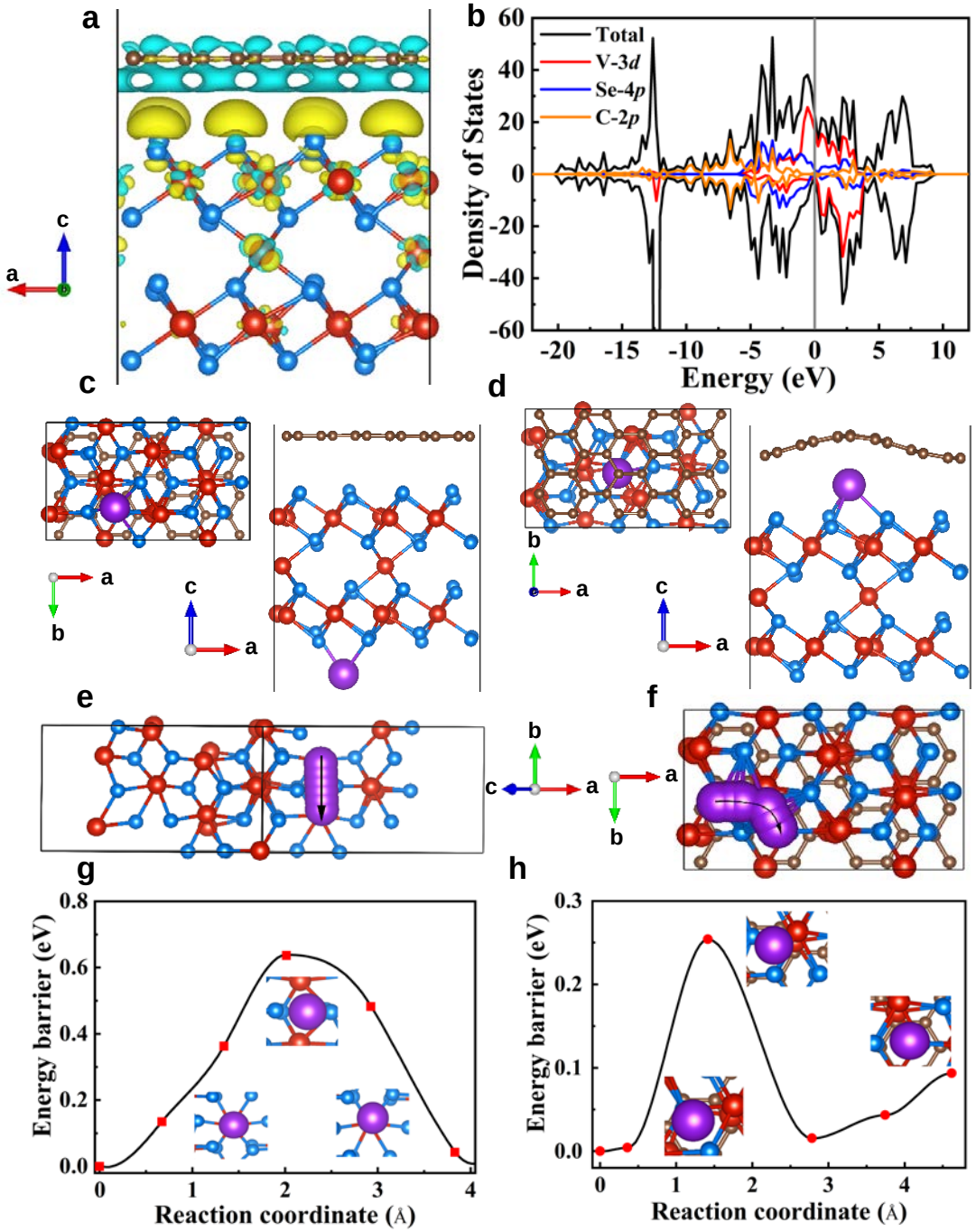

Figure 4. (a) The charge density difference of V_5Se_8/Gr interface, where blue represents charge depletion and yellow indicates charge accumulation. (b) The total density of states and projected density of states of V_5Se_8/Gr interface. Stable structures of K adsorption (c) at the interface sites of V_5Se_8/Gr and (d) on the surface of V_5Se_8 in V_5Se_8/Gr interface. The K diffusion path (e) and diffusion energy barrier (g) in bulk V_5Se_8. K diffusion on V_5Se_8 surface in V_5Se_8/Gr interface system: (f) diffusion path and (h) energy barrier.

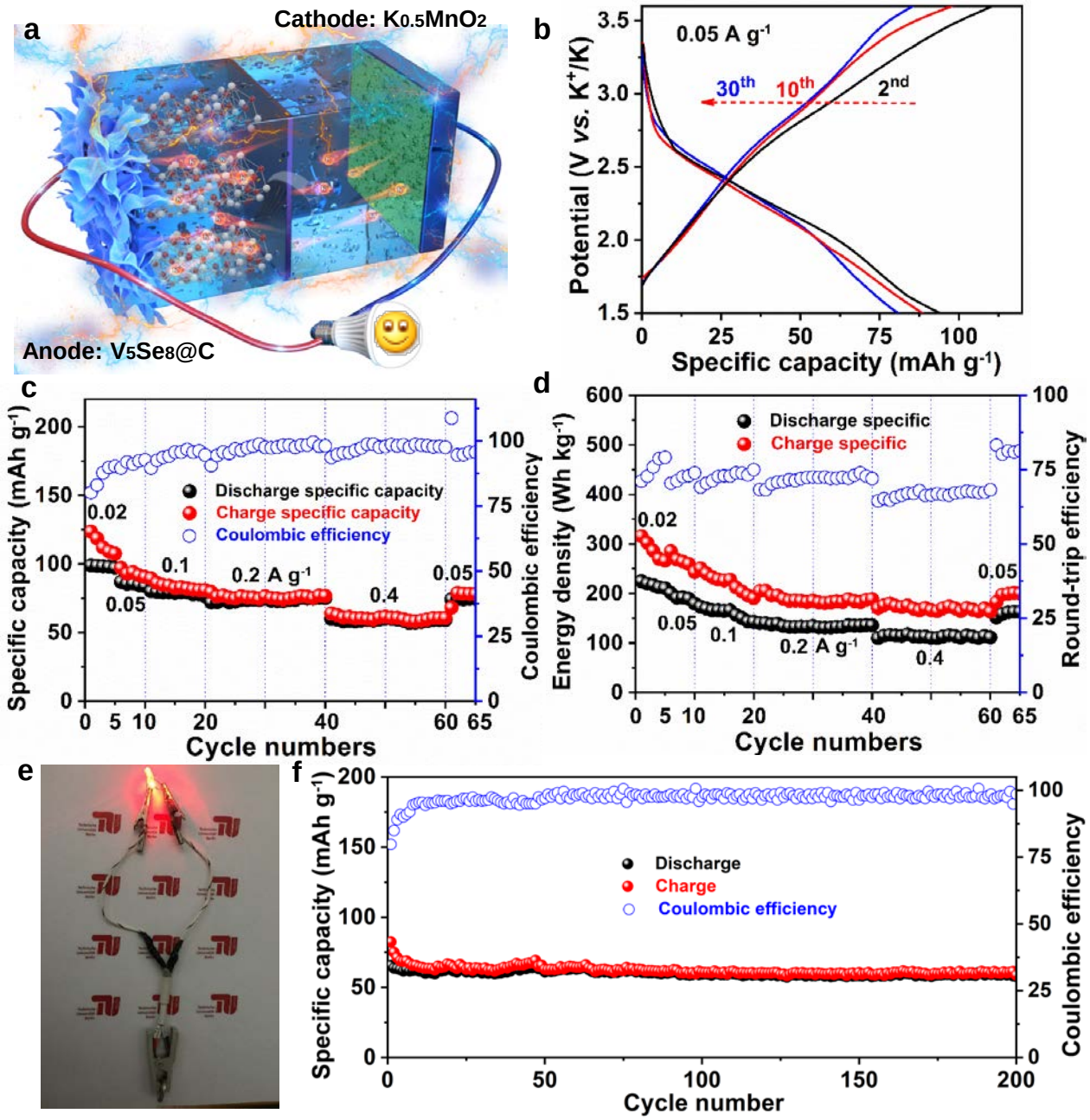

Figure 5. (a) Schematic illustration of the $K_{0.5}MnO_2$//V_5Se_8@C nanosheets K-ion full battery. (b) Charge/discharge curves the as-fabricated full cell at 0.05 A g^{-1} in the voltage range of 1.50−3.60 V (*vs.* K^+/K). (c) Variation in rate performances and the corresponding CE of the full cell under different current densities. (d) Energy density and round-trip efficiency of the $K_{0.5}MnO_2$//V_5Se_8@C full-cell at different current densities. (e) Digital photo of two LED lights powered by one full cell after a long-term cycling. (f) Cyclic performance and the corresponding CE at 0.4 A g^{-1}.

Graphic Abstract

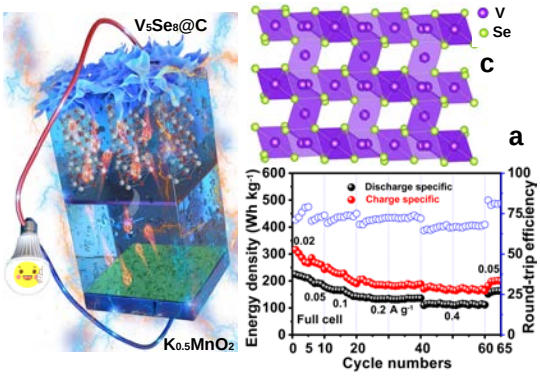

We report the first example of designing ultrathin metallic V_5Se_8 nanosheets embedded in porous carbon layer for greatly boosting the performance of K-ion batteries in terms of capacity, rate capability and cycling stability.